Optimization of photorefractive two-wave mixing by accounting for material anisotropies: $KNbO_3$ and $BaTiO_3$

Germano Montemezzani
Nonlinear Optics Laboratory, Swiss Federal Institute of Technology, ETH Hönggerberg HPF, 8093 Zürich, Switzerland
(Received 11 April 2000; published 11 October 2000)

The influence of the anisotropy of the effective dielectric constant, effective electro-optic effect, drift mobility, and photoexcitation cross section on the photorefractive two-wave mixing gain and speed are analyzed in detail. Theoretical expressions that include all these influences and that are valid for the single-level band model are reported. They can give the necessary guidance for optimizing the interaction geometries and the extrinsic crystal properties for systems based on two- and four-wave mixing or self-pumped phase conjugation. Concrete examples are given for $KNbO_3$ and $BaTiO_3$, where all possible two-beams interaction geometries are analyzed in the plane of maximum photorefractive nonlinearity (bc and ac plane, respectively). It is shown that, besides the dielectric constant and the electro-optic effect, also the anisotropy of the photoexcitation with respect to wave polarization plays a major role and strongly influences the optimum geometry, allowing potentially very large enhancement of the exponential gain. Corrections to the standard expressions for photorefractive two-wave mixing amplification in the depleted pump regime are also given. They apply in the case of asymmetric incidence and/or under the presence of anisotropic photoexcitation.

PACS number(s): 42.40.Pa, 42.70.Nq, 42.70.Mp

I. INTRODUCTION

The photorefractive effect [1,2] can be viewed as a combination of three physical processes: charge photoexcitation, charge transport, and the electro-optic effect. Upon inhomogeneous illumination of a photorefractive material the former two processes give rise to an inhomogeneous bulk charge distribution, which is then translated into a modulation of the refractive index by the latter effect. The physical and optical material properties of inorganic and organic materials involved in the above processes are often strongly anisotropic. Three important kinds of anisotropy can be identified. First, the magnitude of the electro-optic effect and of the low-frequency dielectric constant depend on the direction of the internal space-charge field and, specially in inorganic crystals, is strongly affected by mechanical coupling within the material. Second, charge transport, i.e., carrier mobilities, can differ significantly for different drift directions. Finally, photoexcitation cross sections can be anisotropic with respect to wave polarization. All these anisotropic material properties influence either the magnitude of the charge modulation being created or the speed of its formation, or the coupling of the charge modulation to the optical properties, or a combination of these effects.

Many of the most common applications of photorefractive materials, such as phase conjugation [3], dynamic holographic interferometry [4], or laser beam combining [5] rely directly or indirectly on a two-wave mixing process. Optimization of the performance for a given material usually requires finding an optimum beam interaction geometry, which, obviously, also depends on the intrinsic or extrinsic anisotropic parameters of the material.

In this work we discuss in detail the effects on the photorefractive performance, i.e., on the photorefractive two-wave mixing gain, response time, and sensitivity, that are brought about by material anisotropies. The expressions given below can be used for any nonoptically active photorefractive crystal. Detailed practical examples are given for the two important crystals $KNbO_3$ and $BaTiO_3$, whose properties are fully characterized. Earlier works concerned with geometry optimization of these two crystals did not take into account all possible sources of material anisotropies [6–8] and none of them considered the effect of the photoexcitation anisotropy. In addition, several of the relevant material parameters necessary to characterize the amount of piezoelectric coupling and the charge transport anisotropy have been experimentally determined with high precision in the last few years [9–13]. In $KNbO_3$ and $BaTiO_3$ the optimum configurations for two-wave mixing are with the interacting beams in the crystallographic bc plane and ac plane, respectively. Therefore we limit our discussions to all possible interaction geometries in these planes. It is shown that for a given trap concentration, the geometry giving maximum gain is a function of the anisotropy of the photoexcitation constant. This property can be used, for example, for identifying geometries with large gain but small linear scattering from the pump to the signal beam.

The paper is constructed as follows. In Sec. II we treat the dependence of the effective static dielectric constant and effective scalar electro-optic coefficient on the interaction geometries. The angular dependence of the drift mobility is discussed in Sec. III, while the anisotropy of the photoexcitation and its important influence on the charge modulation is analyzed in Sec. IV. Section V discusses the combined effects of all these anisotropies on photorefractive two-wave mixing. The undepleted and depleted pump regimes are both analyzed in detail. Finally Sec. VI discusses the effect brought about by the anisotropies on the photorefractive response time and two-wave mixing sensitivity.

II. STATIC DIELECTRIC CONSTANT AND ELECTRO-OPTIC EFFECT

It is well known that the static dielectric tensor and the electro-optic tensor are of anisotropic nature for most of the

point groups, to whom the major photorefractive crystals belong. This anisotropy is obvious and, to our knowledge, it is taken into account in all works aimed at optimizing photorefractive geometries. However, as pointed out by several researchers [14–17], the magnitude of the effective dielectric constant and electro-optic coefficient being active in a particular experiment does not depend only on this primary tensor properties. The mechanical state of the crystal also plays a major role. It could be shown that, in general, an electro-optic crystal containing a sinusoidal electric-field grating modulation is neither in a mechanically free, nor in a mechanically totally clamped state. In fact, some of the possible local mechanical relaxation in response to the periodic electric field are allowed, while others are clamped. As a consequence the magnitude of the dielectric response results from a combination of several contributions involving the piezoelectric effect and the material elasticity. To calculate the electro-optic response also the elasto-optic properties should be added to the picture.

Following Ref. [16] the effective scalar dielectric constant ε_{eff} that relates the amplitude ρ_0 of the sinusoidally modulated space-charge density to the amplitude $E_{sc,0}$ of the modulated space-charge electric field is calculated as

$$\varepsilon_{eff}=\frac{\rho_0}{\varepsilon_0 K E_{sc,0}}=\hat{K}_i\hat{K}_j\left[\varepsilon_{ij}^S+\frac{1}{\varepsilon_0}e_{ijk}A_{kl}^{-1}B_l\right], \tag{1}$$

where summation over equal indexes is assumed, and A_{kl}^{-1} is the inverse matrix of

$$A_{lk}\equiv C_{lmkn}^E\hat{K}_m\hat{K}_n, \tag{2}$$

the vector B_l is defined as

$$B_l\equiv e_{plq}\hat{K}_p\hat{K}_q, \tag{3}$$

and the other quantities are $\hat{K}_i$, the Cartesian component i of the unit vector parallel to the grating vector $\vec{K}$; ε_{ij}^S, the clamped static dielectric tensor; ε_0, the permittivity of vacuum; e_{ijk}, the piezoelectric stress tensor; and C_{lmkn}^E, the elastic stiffness tensor at constant electric field. For a known grating direction $\hat{K}$ the change in the refractive index ellipsoid may be expressed in terms of an effective second-rank electro-optic tensor r_{ij}^{eff} [9] and of the scalar amplitude E_{sc} as

$$\Delta\left(\frac{1}{n^2}\right)_{ij}\equiv r_{ij}^{eff}E_{sc}, \tag{4}$$

where r_{ij}^{eff} is calculated as [16]

$$r_{ij}^{eff}=r_{ijk}^S\widehat{K_k}+p_{ijkl}'^E\widehat{K_l}A_{km}^{-1}B_m, \tag{5}$$

with r_{ijk}^S being the clamped (third-rank) electro-optic tensor and $p_{ijkl}'^E$ being the modified elasto-optic tensor at constant electric field, this tensor contains also the roto-optic contributions [18]. In a given experimental configuration one is rather interested in a scalar effective electro-optic coefficient r_{eff}. This quantity is proportional to the refractive index modulation Δn seen by the two interacting waves and is defined as

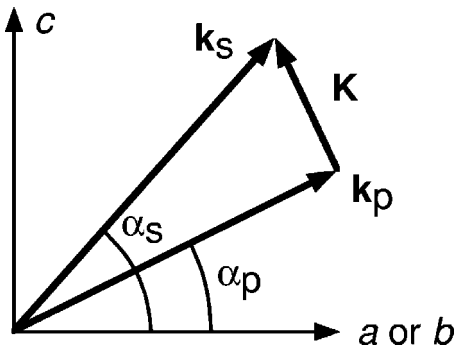

FIG. 1. Angle convention used in this work. All angles are in the ac ($BaTiO_3$) or bc crystal plane ($KNbO_3$) and are internal to the crystal.

$$r_{eff}\equiv\widehat{d_i^S}r_{ij}^{eff}\widehat{d_j^P}, \tag{6}$$

where $\widehat{d^P}$ ($\widehat{d^S}$) are the unit vectors pointing in the direction of the electric displacement (polarization) for the interacting pump (P) and signal (S) wave, respectively. The relationship between r_{eff} and two-wave mixing gain coefficient Γ will be given below, while the relationship with the diffraction efficiency for Bragg-diffraction experiments can be found in Ref. [19].

As it appears evident from Eqs. (1), (2), (3), and (5), a large number of material constants must be known in order to calculate the active value of ε_{eff} and r_{eff}. For the materials $KNbO_3$ and $BaTiO_3$ the whole set of dielectric, elastic, electro-optic, piezoelectric, and elasto-optic constant has been determined [9,10]. Throughout this paper the expected performance characteristics of these two materials will be described for all possible two-wave interaction angles in the optimum incidence plane (the bc plane for $KNbO_3$, the ac plane for $BaTiO_3$). Figure 1 shows the convention taken for the angles of interaction. The angles α_S and α_P are internal to the crystal and represent the angles between the wave vector $\vec{k}$ of the signal and pump waves and the crystallographic a axis ($BaTiO_3$) or b axis ($KNbO_3$). Since the largest electro-optic coefficients are accessed only for p polarization of the waves, we consider here only this situation. The case of s polarization is much less interesting and gives significantly smaller gains in our two crystals.

Figure 2 shows a contour plot giving the effective scalar electro-optic coefficient r_{eff} for the bc-plane interaction in $KNbO_3$ as calculated from Eqs. (2), (3), (5), and (6). The values are calculated for the wavelength $\lambda=515$ nm using the material data given in [20]. The thick lines connect points for which the effective electro-optic coefficient vanishes while the positions of the peak values are indicated by triangles. Solid contour lines connect points with a positive

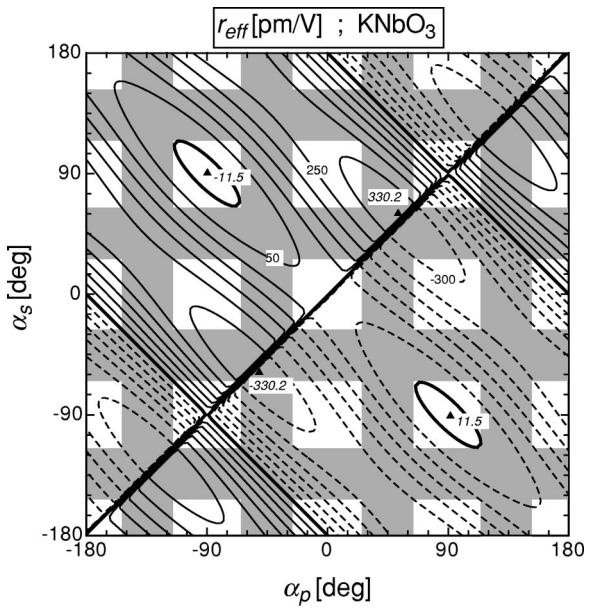

FIG. 2. Contour plot of the scalar effective electro-optic coefficient r_{eff} [Eq. (6)] for each possible two-wave interaction geometry (α_p,α_s) in the bc plane of $KNbO_3$. Shadowed regions correspond to internal angles which are not accessible from air with a conventional crystal cut along the three crystallographic axes. The contour line distance is 50 pm/V, dashed lines represent negative values, and the thick solid line connects points with $r_{eff}=0$. Triangles denote the position of local or global maxima or minima (italic values).

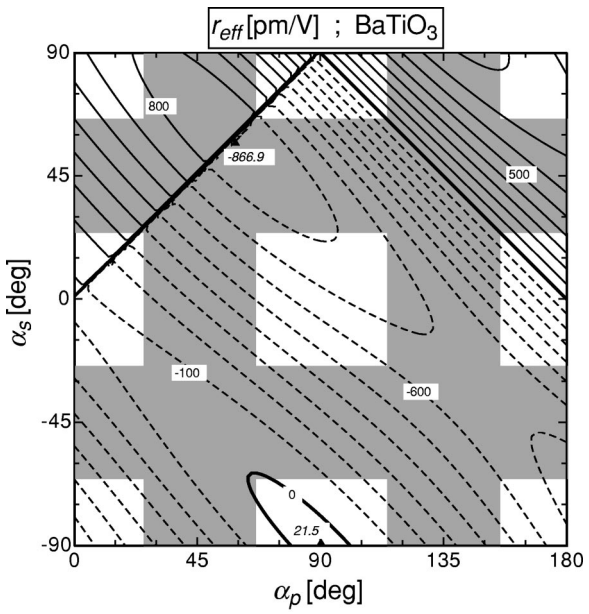

FIG. 3. Contour plot of the scalar effective electro-optic coefficient r_{eff} [Eq. (6)] for each possible two-wave interaction geometry (α_p,α_s) in the ac plane of $BaTiO_3$. Reduced representation containing all nonredundant information (see text). The contour line distance is 100 pm/V. For the meaning of shadows and special symbols see Fig. 2.

value of the represented quantity, while dashed contour lines indicate negative values. The shadowed areas indicate angular regions which, as a result of Snellius law, cannot be directly accessed from air in a crystal with the surfaces cut perpendicular to the crystallographic b and c axes. However, these regions may be accessed for other crystal cuts or by using external wedges. For instance, by cutting a crystal sample under 45° with respect to the crystallographic axes the whole shadowed area is accessible. Note that the magnitude of r_{eff} and the contour lines shape differ significantly from the expected values in the case where the mechanical coupling effects included in Eqs. (2), (3), (5), and (6) would have been neglected.

From Fig. 2 it appears evident that a few symmetry operations apply to such a diagram. First of all the diagram is invariant upon point symmetry on each of the four points $(\alpha_P,\alpha_S)=(-90°,-90°)$, $(90°,-90°)$, $(-90°,90°)$, or $(90°,90°)$. Executing these point symmetry operations corresponds in the laboratory frame to a rotation of the crystal by 180° around the crystallographic c axis (exchange of b with $-b$), which leaves the effects unchanged. The other symmetry operation is an inversion of all values upon point symmetry on the central point $(\alpha_P,\alpha_S)=(0°,0°)$. This symmetry operation corresponds to a rotation of the crystal by 180° around the b axis (a axis for $BaTiO_3$), i.e., to a switch of the direction of the polar c axis which reverses the sign of the optical nonlinearity. Note that the inversion with respect to mirroring at the main diagonal seen in Fig. 2 (exchange of angles between pump and signal wave) is not a general symmetry operation and does not hold for all quantities that will be discussed in this work.

By making use of the symmetries discussed above all redundant information can be eliminated and the size of the diagram of Fig. 2 can be reduced by a factor of 4. As an example, Fig. 3 shows the reduced contour plot diagram for r_{eff}, this time for the ac plane of $BaTiO_3$. A scalar electro-optic coefficient of the order of 800 pm/V can be accessed even for conventional crystal cuts. In Fig. 3 the angles α_p and α_S have been chosen to vary in the intervals $[0°,180°]$ and $[-90°,90°]$, respectively. This choice will be maintained for the rest of this work. In this representation all conventional geometries for which the grating vector $\vec{K}$ is parallel to the c axis are found along the diagonal connecting the points $(90°,-90°)$ and $(0°,0°)$. All geometries with the two beams exactly counterpropagating are found along the diagonal connecting the points $(90°,-90°)$ and $(180°,0°)$, with the grating vector turning from the c to the a (or b) axis while proceeding along the line. Along the diagonal connecting the points $(180°,0°)$ and $(90°,90°)$ the grating vector points along the $a(b)$ axis and no electro-optic coupling exists. Finally, along the last side diagonal $[(0°,0°)$ to $(90°,90°)]$ the grating vector always vanishes and so does the effective scalar electro-optic coefficient.

As seen in Eq. (1) the effective dielectric constant depends only on the direction of the grating vector $\hat{K}$, and not on the individual polarization vectors of the two interacting waves. Therefore, in a diagram such as the one of Fig. 3, besides for small corrections due to birefringence, the contour lines for ε_{eff} are all essentially parallel to the diagonal going from top left to bottom right. Keeping that in mind we

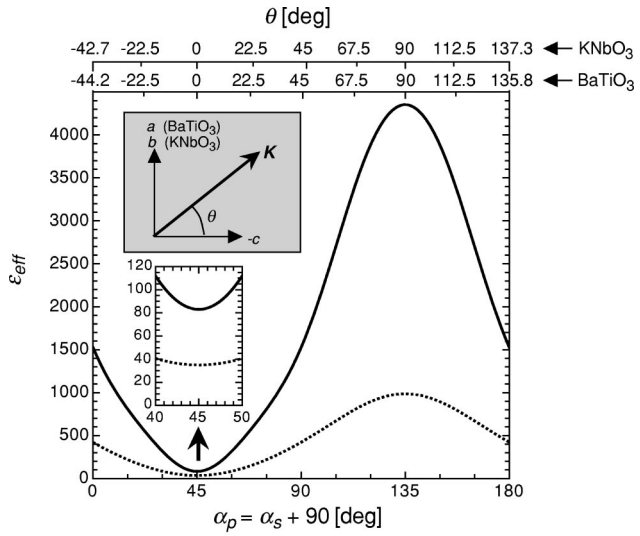

FIG. 4. Effective dielectric constant ε_{eff} [Eq. (1)] measured along the main diagonal (bottom left to top right) of a diagram such as the one of Fig. 3 for $BaTiO_3$ (solid curve) and $KNbO_3$ (dotted curve). The values of ε_{eff} remain essentially constant by moving away from the main diagonal in normal direction [i.e., $\varepsilon_{eff}(\alpha_p \pm \beta, \alpha_s \mp \beta) \simeq \varepsilon_{eff}(\alpha_p, \alpha_s)$]. The top axis shows the grating angle θ defined in the inset.

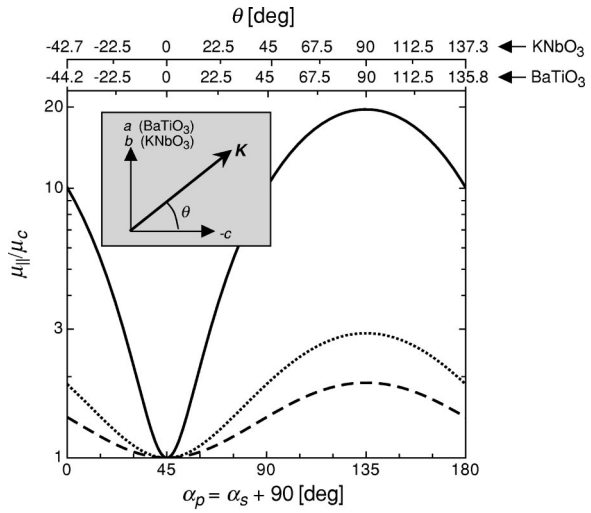

FIG. 5. Normalized component $\mu_{||}/\mu_c$ [Eq. (7)] of the drift mobility which is parallel to the grating vector $\hat{K}$. The curves are for hole-conducting $BaTiO_3$ (solid curve), hole-conducting $KNbO_3$ (dotted curve), and electron-conducting $KNbO_3$ (dashed curve). As in Fig. 4, the values are for a cut along the main diagonal of a contour profile diagram such as the one of Fig. 3. It holds that $\mu_{||}/\mu_c(\alpha_p \pm \beta, \alpha_s \mp \beta) \simeq \mu_{||}/\mu_c(\alpha_p, \alpha_s)$.

choose to plot the values of ε_{eff} in a conventional diagram while we move solely along the main diagonal (from left bottom to top-right) in Fig. 3. This is shown in Fig. 4 for both crystals under consideration. An extremely strong dependence of the dielectric constant on the interaction geometry is evident. For completeness the top axes in Fig. 4 give also the angular direction θ of the corresponding grating vector $\hat{K}$ for the two crystals. These axes are slightly nonlinear with respect to the bottom one as a result of the material birefringence.

III. CARRIER DRIFT MOBILITY

In general, in anisotropic materials the carrier drift velocity vector $\vec{v}$ is not necessarily parallel to the electric field $\vec{E}$ driving the charges and the two quantities are related by a tensorial drift mobility $\vec{v} = \vec{\vec{\mu}} \cdot \vec{E}$. In photorefractive experiments performed in ideal infinitely large crystals any charge movement in a direction perpendicular to the grating vector $\hat{K}$ does not lead to charge separation because the light energy is homogeneous along such directions. Therefore one is interested only in the component of the drift velocity parallel to the modulated field $\vec{E}$, i.e., parallel to $\hat{K}$. The scalar (parallel) effective drift mobility $\mu_{||}$ can then be easily calculated as

$$\mu_{||} = \widehat{K} \cdot \vec{\vec{\mu}} \cdot \widehat{K} = \mu_c \left(\cos^2 \theta + \frac{\mu_{a,b}}{\mu_c} \sin^2 \theta \right), \qquad (7)$$

where the second equality holds for our specifically considered geometries and the angle θ is defined as in Fig. 4.

The ratios $\mu_{a,b}/\mu_c$ of the carrier mobilities active in a photorefractive experiment are best determined using holographic techniques as performed in Refs. [11–13] for $BaTiO_3$ and $KNbO_3$. Using the most recent data for hole-conducting $BaTiO_3$ and electron- and hole-conducting $KNbO_3$ reported in [13], the ratio $\mu_{||}/\mu_c$ is plotted in Fig. 5 in the same kind of representation employed for Fig. 4. In both crystals the mobility is largest for a drift direction perpendicular to the polar axis. In $BaTiO_3$ the maximum mobility ratio reaches a factor of 20. Note that while the absolute values of the effectively observed mobility may be influenced by trapping effects and the observation time scale, the ratio between the mobility in different directions is not.

IV. PHOTOEXCITATION CONSTANT

In doped photorefractive crystals photoexcitation is in general an extrinsic property of the material. It is not uncommon that the probability for a carrier to be photoexcited to the conduction or valence band depends on the polarization of the incident photons. If such a dependence exists, the complex amplitude $E_{sc,0}$ of the modulated photoinduced internal electric field $\vec{E}_{sc}(\vec{r}) = \hat{K} E_{sc,0} \exp(i\vec{K}\vec{r})$ is strongly influenced and differs significantly from what would be expected on the base of the light intensity distribution [21]. This is because it is the modulation m of the photoexcited free carriers and not the light intensity modulation that drives the formation of the space-charge field. For two interacting beams for which the electric field vectors have the form $\vec{\epsilon}_S(\vec{r},t) \equiv E_S(\vec{r}) \widehat{e^S} \exp[i(\vec{k}_S \cdot \vec{r} - \omega t) - \alpha_S \hat{\zeta} \cdot \vec{r}]$ (signal wave) and $\vec{\epsilon}_P(\vec{r},t) \equiv E_P(\vec{r}) \widehat{e^P} \exp[i(\vec{k}_P \cdot \vec{r} - \omega t) - \alpha_P \hat{\zeta} \cdot \vec{r}]$ (pump wave), the photoexcited free carriers modulation is expressed as [19]

$$m(\vec{r})=\frac{2E_S(\vec{r})E_P^*(\vec{r})[\widehat{e^S}\cdot\vec{\kappa}\cdot\widehat{e^P}]e^{-(\alpha_S+\alpha_P)\hat{\zeta}\cdot\vec{r}}}{|E_P(\vec{r})|^2[\widehat{e^P}\cdot\vec{\kappa}\cdot\widehat{e^P}]e^{-2\alpha_P\hat{\zeta}\cdot\vec{r}}+|E_S(\vec{r})|^2[\widehat{e^S}\cdot\vec{\kappa}\cdot\widehat{e^S}]e^{-2\alpha_S\hat{\zeta}\cdot\vec{r}}}, \tag{8}$$

where $\hat{\zeta}$ is a unit vector normal to the entrance surface of the beams in the crystal and α_S and α_P are the amplitude absorption constants for the two waves as measured along this direction [19]. The second-rank tensor $\vec{\kappa}$ describes the anisotropy of the photoexcitation process and is related to the absorptive part of the dielectric tensor, i.e., to the symmetric imaginary part $\overleftrightarrow{\varepsilon''}$ of the complex material dielectric tensor $\vec{\varepsilon}=\overleftrightarrow{\varepsilon'}+i\overleftrightarrow{\varepsilon''}$. It is defined as

$$\kappa_{kl}\equiv\phi_{kl}(\varepsilon'')_{kl}, \tag{9}$$

where the quantities ϕ_{kl} describe the light polarization dependence of the quantum efficiency, that is, the probability that an absorbed photon of given polarization produces a photoexcited mobile carrier. Note that in Eq. (9) no summing over equal indices is performed. Note also that the photoexcited free-carrier modulation (8) is obtained by evaluating the modulation of the optical energy density

$$w(\vec{r})=w_0\,\mathrm{Re}[1+m\exp(i\vec{K}\vec{r})], \tag{10}$$

which is dissipated in a useful way for the process of interest, i.e., is used to generate movable free carriers. The quantity $w(\vec{r})$ is expressed as

$$w(\vec{r})=\frac{1}{2}\varepsilon_0[\vec{\epsilon}(\vec{r})\cdot\vec{\kappa}\cdot\vec{\epsilon}^*(\vec{r})], \tag{11}$$

where ε_0 is the permittivity of vacuum and $\vec{\epsilon}(\vec{r})=\vec{\epsilon}_S(\vec{r})+\vec{\epsilon}_P(\vec{r})$ is the complex amplitude of the total optical electric field obtained by the coherent superposition of the signal and pump wave.

As we will see in the next section, an anisotropy of the photoexcitation process, i.e., an anisotropy of the tensor $\vec{\kappa}$, has a dramatic effect on the value of the exponential gain coefficient Γ in photorefractive two-wave mixing experiments.

V. PHOTOREFRACTIVE TWO-WAVE MIXING

Under the slowly varying amplitude approximation the coupled-wave equations describing the interaction between the signal (S) and the pump wave (P) in a photorefractive two-wave mixing process in anisotropic materials are [19]

$$\vec{\nabla}E_S\cdot\hat{u}_S=\frac{k_0}{4n_Sg_S}[-iRmE_P\tilde{E}_{sc,0}e^{(\alpha_S-\alpha_P)\hat{\zeta}\cdot\vec{r}}], \tag{12a}$$

$$\vec{\nabla}E_P\cdot\hat{u}_P=\frac{k_0}{4n_Pg_P}[-iRm^*E_S\tilde{E}^*_{sc,0}e^{(\alpha_P-\alpha_S)\hat{\zeta}\cdot\vec{r}}], \tag{12b}$$

where $R\equiv n_S^2n_P^2g_Sg_Pr_{eff}$, and n_S (n_P) are the refractive index seen by the signal (pump) waves, respectively, $g_S\equiv\widehat{e^S}\cdot\widehat{d^S}$ and $g_P\equiv\widehat{e^P}\cdot\widehat{d^P}$ are projection factors, r_{eff} is given by Eq. (6), $\hat{u}_S$ ($\hat{u}_P$) are unit vectors in direction of the Poynting vectors of the waves S and P, respectively, $k_0=2\pi/\lambda$ is the free space wave vector for the wavelength λ, and $\tilde{E}_{sc,0}\equiv E_{sc,0}/m=\tilde{E}_{sc,r}+i\tilde{E}_{sc,i}$ is the complex amplitude of the first Fourier component of the internal space-charge field normalized by the modulation m. Its real part $\tilde{E}_{sc,r}$ corresponds to the component of the space-charge field being in phase with the energy density distribution (10), while the imaginary part $\tilde{E}_{sc,i}$ is the $\pi/2$ out-of-phase component. Finally, the remaining quantities E_S, E_P, m, $\hat{\zeta}$, α_P, and α_S in Eq. (12) were defined in Sec. IV.

A. Undepleted pump approximation

In the undepleted pump approximation the energy of the pump wave is always much larger than the one of the signal wave, i.e., $|E_P|^2[\widehat{e^P}\cdot\vec{\kappa}\cdot\widehat{e^P}]\exp(-2\alpha_P\hat{\zeta}\cdot\vec{r})\gg|E_S|^2[\widehat{e^S}\cdot\vec{\kappa}\cdot\widehat{e^S}]\exp(-2\alpha_S\hat{\zeta}\cdot\vec{r})$. In this case equations (12) describing the evolution of the signal-wave amplitude transforms to

$$\vec{\nabla}E_S\cdot\hat{u}_S=\frac{k_0R}{4n_Sg_S}\frac{\widehat{e^S}\cdot\vec{\kappa}\cdot\widehat{e^P}}{\widehat{e^P}\cdot\vec{\kappa}\cdot\widehat{e^P}}[\tilde{E}_{sc,i}-i\tilde{E}_{sc,r}]E_S, \tag{13}$$

which can be easily solved for E_S leading to

$$E_S(\hat{\zeta}\cdot\vec{r}=d)=E_{S0}e^{(\Gamma/2)d}e^{i\delta d}, \tag{14}$$

or

$$|\vec{\epsilon}_S|(\hat{\zeta}\cdot\vec{r}=d)=|\vec{\epsilon}_{S0}|e^{(\Gamma/2-\alpha_S)d}, \tag{15}$$

where E_{S0} and $\vec{\epsilon}_{S0}$ are the corresponding incident amplitudes at the position $\hat{\zeta}\cdot\vec{r}=0$; here it is assumed that the entrance surface (surface where the wave S starts interacting with P) contains the coordinates origin. The two-wave mixing exponential gain Γ and the phase coupling factor δ in Eq. (14) are given by

$$\Gamma=\frac{2\pi}{\lambda}\frac{n_Sn_P^2}{\cos\theta_S}g_P\frac{\widehat{e^S}\cdot\vec{\kappa}\cdot\widehat{e^P}}{\widehat{e^P}\cdot\vec{\kappa}\cdot\widehat{e^P}}r_{eff}\tilde{E}_{sc,i}, \tag{16}$$

and

$$\delta=-\frac{\pi}{\lambda}\frac{n_Sn_P^2}{\cos\theta_S}g_P\frac{\widehat{e^S}\cdot\vec{\kappa}\cdot\widehat{e^P}}{\widehat{e^P}\cdot\vec{\kappa}\cdot\widehat{e^P}}r_{eff}\tilde{E}_{sc,r}, \tag{17}$$

where $\cos\theta_S = \hat{\xi}\cdot\hat{u}_S$ is the cosine of the angle between the Poynting vector and the surface normal. As seen in Eq. (16) the exponential gain depends on the photoexcitation anisotropy through the factor $(\widehat{e^S}\cdot\vec{\kappa}\cdot\widehat{e^P}/\widehat{e^P}\cdot\vec{\kappa}\cdot\widehat{e^P})$. If the tensor $\vec{\kappa}$ is sufficiently anisotropic, by choosing appropriate geometries this factor can become very large with respect to 1, thus giving an enhancement of the two-wave mixing gain. The dependence of the gain on the factor accounting for the photoexcitation anisotropy has been confirmed experimentally using dichroic $KNbO_3$ [21].

In order to predict the magnitude of Γ and δ in a particular geometry the knowledge of the values of $\tilde{E}_{sc,i}$ and $\tilde{E}_{sc,r}$ is necessary. In the undepleted pump approximation, the modulation m is always small and the space-charge field amplitude is linearly proportional to m. Therefore the normalized amplitudes $\tilde{E}_{sc,i}$ and $\tilde{E}_{sc,r}$ do not depend at all on m in this regime. Here we limit our considerations to the predictions of the simplest and most recognized photorefractive model that considers a single defect level and a single carrier type [22]. Under the assumptions of a negligible photogalvanic effect (which is usually the case in most $KNbO_3$ and $BaTiO_3$ samples) and assuming that no external electric field is applied, the normalized space-charge field amplitude $\tilde{E}_{sc,0}$ is [22]

$$\tilde{E}_{sc,0} = \pm i\frac{E_q E_D}{E_q + E_D}, \tag{18}$$

and therefore $\tilde{E}_{sc,r}=0$ under these assumptions. In Eq. (18) the $+$ sign holds for hole conduction and the $-$ sign holds for electron charge transport. The real trap-limited field E_q and diffusion-limited field E_D are defined as $E_q \equiv (e/\varepsilon_0\varepsilon_{eff}|\vec{K}|)N_{eff}$ and $E_D \equiv |\vec{K}|k_BT/e$, where e is the elementary charge, k_B is the Boltzmann constant, T is the absolute temperature, N_{eff} is the effective density of traps, and ε_{eff} is given by Eq. (1). Equation (18) predicts the space-charge field amplitude in most photorefractive materials in a satisfactory way and will be used here to visualize the geometrical dependence of the gain Γ. Several refined models that describe better the space-charge formation in specific situations or in specific crystal samples have been reported in literature, for a review see for instance Ref. [23]. Note that effects such as electron-hole competition or multiple defect levels usually tend to decrease the space-charge field strength and, given a trap density, Eq. (18) can be viewed as an upper bound for the space-charge field amplitude.

In order to visualize the dependence of the exponential gain Γ in $KNbO_3$ and $BaTiO_3$ on the geometrical arrangement and on the anisotropy of the tensor $\vec{\kappa}$ we use the same kind of contour plot representation as in Fig. 3. Using Eqs. (16) and (18) in Figs. 6(a)–6(c) we plot the $KNbO_3$ gain contour plot diagrams for $\kappa_{22}/\kappa_{33}=1$ (isotropic case), $\kappa_{22}/\kappa_{33}=0.1$, and $\kappa_{22}/\kappa_{33}=100$, respectively. Figures 7(a)–7(c) show the same for $BaTiO_3$. In each case the effective number of traps is chosen to be $N_{eff}=10^{17}$ cm^{-3} and hole conduction is assumed. The gain plotted here is given per unit length along the Poynting vector direction; that is, it

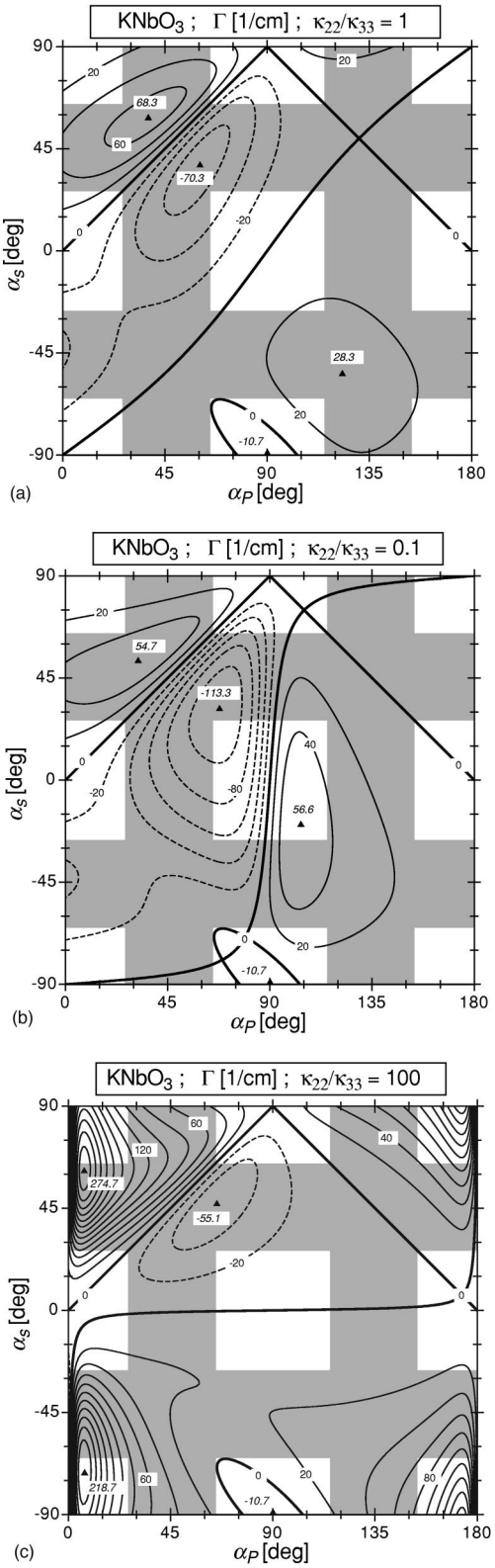

FIG. 6. Contour plot of the exponential gain $\Gamma\cos\theta_s$ [Eq. (16)] for p-polarized beams in the bc plane of $KNbO_3$. (a) Isotropic photoexcitation, $\kappa_{22}/\kappa_{33}=1$; (b) anisotropic photoexcitation $\kappa_{22}/\kappa_{33}=0.1$; (c) $\kappa_{22}/\kappa_{33}=100$. The contour line distance is 20 cm^{-1}. Effective density of traps $N_{eff}=10^{17}$ cm^{-3}. For the meaning of shadows and special symbols see Fig. 2.

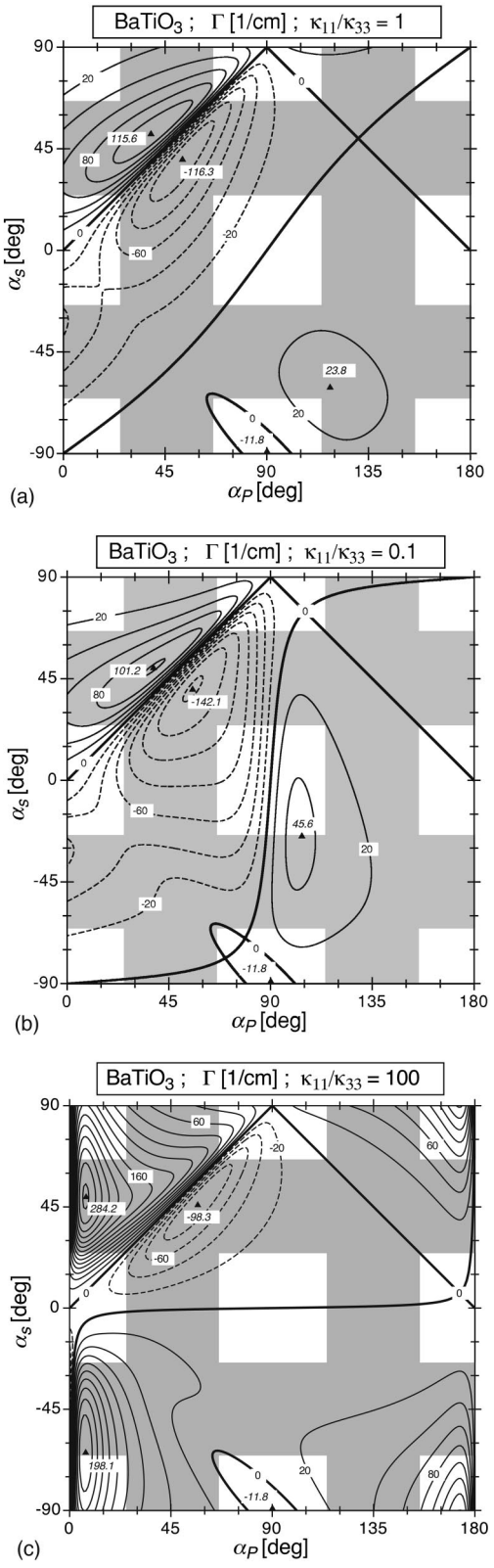

FIG. 7. Contour plot of the exponential gain $\Gamma\cos\theta_s$ [Eq. (16)] for *p*-polarized beams in the *ac* plane of $BaTiO_3$. (a) Isotropic photoexcitation, $\kappa_{11}/\kappa_{33}\equiv\kappa_{22}/\kappa_{33}=1$; (b) anisotropic photoexcitation $\kappa_{11}/\kappa_{33}=0.1$; (c) $\kappa_{11}/\kappa_{33}=100$. The contour line distance is 20 cm^{-1}. Effective density of traps $N_{eff}=10^{17}$ cm^{-3}.

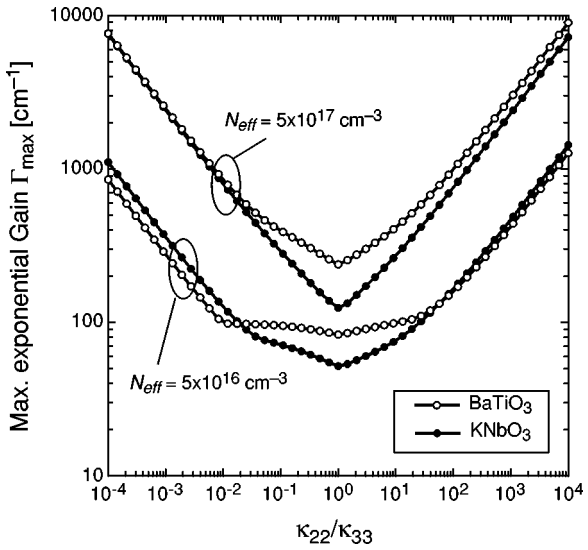

FIG. 8. Maximum exponential gain $\Gamma\cos\theta_s$ as a function of the photoexcitation anisotropy parameter κ_{22}/κ_{33}. Each point was determined by finding the peak value over all possible two-wave mixing interaction geometries.

corresponds to $\Gamma\cos\theta_s$ [see Eq. (16)]. In this way, the representation becomes independent from a specific crystal cut. From Figs. 6 and 7 it becomes evident that the gain landscape is dramatically modified by the anisotropy of the photoexcitation constant. The position of the maximum gain in the diagram moves by changing the parameter κ_{22}/κ_{33}; some of the mountains grow, while others decrease in height. For $\kappa_{22}/\kappa_{33}\gg 1$ the optimum condition is found for a pump beam propagating under an angle α_p close to 0°, that is nearly perpendicular to the *c* axis. In contrast, for $\kappa_{22}/\kappa_{33}\ll 1$ the optimum is for a pump beam nearly parallel to *c*.

It is worth noticing that by assuming an initial light scattering distribution, the representations of Figs. 6 and 7 can be used to qualitatively predict the structure of light fanning as well as optimum configurations for various phase conjugation schemes. For a rigorous treatment, however, the knowledge of the two-wave mixing gain alone is not sufficient because grating competition effects have to be taken into account. A detailed discussion of each individual experimental scheme spreads the aim of this paper. We would also like to mention that the above contour diagrams can be easily extended to interaction planes other than the *bc* or *ac* plane, repectively. As an example, the experimentally observed enigmatic fanning distribution observed in $BaTiO_3$ is found to be a direct consequence of the piezoelectric-photoelastic coupling and its anisotropy [24].

It is also interesting to look at the evolution of the maximum possible gain in any geometry as a function of the anisotropy parameter κ_{22}/κ_{33}. This is depicted in Fig. 8 for both crystals and two different values for the trap density. It is evident that the isotropic case represents a kind of worst-case situation, the maximum gain can be enhanced dramatically both by decreasing or increasing the ratio κ_{22}/κ_{33} away from 1. Note that each point in Fig. 8 corresponds to a different position of the maximum in the landscape diagram. It is also worth noting that, despite the fact that $BaTiO_3$ has a

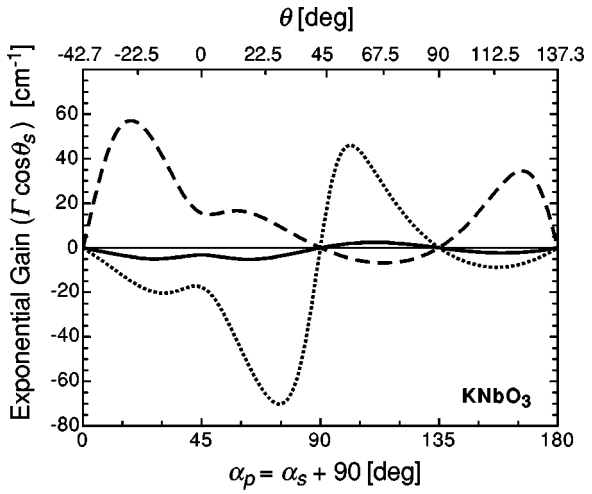

FIG. 9. Exponential gain $\Gamma\cos\theta_s$ in $KNbO_3$ for geometries for which $\vec{k}_s \perp \vec{k}_p$. Dotted curves are for $\kappa_{22}/\kappa_{33}=0.1$, solid curves are for $\kappa_{22}/\kappa_{33}=1$ (isotropic case), and dashed curves are for $\kappa_{22}/\kappa_{33}=10$. $N_{eff}=10^{17}$ cm^{-3}.

maximum scalar electro-optic coefficient almost three times larger than $KNbO_3$ (Figs. 2 and 3), the maximum gains are not significantly higher in this crystal (Fig. 8). This is because of the much larger dielectric constant of $BaTiO_3$ (Fig. 4) that prevents reaching a very high space-charge field $\tilde{E}_{sc,0}$ in some of the geometries where the anisotropy factor in Eq. (16) is big.

For applications, one interesting regime is the one where the pump and signal wave propagate perpendicular to each other because in this regime linear scattering from the pump beam as well as detrimental beam fanning can be minimized. This situation corresponds to the main diagonal in Figs. 6 and 7. Unfortunately, in the absence of photoexcitation anisotropy the gain is very small in such geometries, as seen by the node line in Figs. 6(a) and 7(a) that runs essentially along the main diagonal. This node line is given by the condition $\widehat{e^S}\cdot\vec{\kappa}\cdot\widehat{e^P}=0$ and is substantially modified by the anisotropy of $\vec{\kappa}$ [see, e.g., Figs. 6(b) and 6(c)], thus potentially allowing us to also obtain large gains in this interesting kind of geometry. This is shown in Fig. 9 where the gain coefficient in $KNbO_3$ is plotted for $\vec{k}_s \perp \vec{k}_p$ in the same kind of diagram as in Figs. 4 and 5 for $\kappa_{22}/\kappa_{33}=1$, 0.1, and 10. Note that the situation for $BaTiO_3$ is fully analogous.

B. Pump depletion

If the initial intensity ratio between the pump and signal wave is too low and the gain-length product Γd is large enough the pump wave can be significantly depleted during the two-wave mixing interaction. This situation is more complex than the one found in the weak signal regime. In order to determine the spatial evolution of the signal and pump waves one has then to rely in most cases on a numerical integration of the coupled equations (12). An example is when the two beams enter the crystal from surfaces which are not parallel to each other, in which case the surface normal vectors $\hat{\zeta}_s \neq \hat{\zeta}_p$ and the waves S and P are no longer homogeneous in a direction perpendicular to the corresponding surface normal. It should also be remarked that for a general geometry the absorption constants α_s and α_p for the two waves normally differ from each other (this statement is true even in fully isotropic materials as long as the interaction geometry is not symmetric with respect to the surface normal); therefore also in this case the coupled wave equations may be integrated numerically.

For simplicity we consider here explicitly only cases where the two waves enter the crystal from a common surface or from opposite parallel surfaces. We define the $+z$ direction as being parallel to the direction of the normal to the incidence surface for the S wave $[\hat{\zeta}\equiv\hat{\zeta}_s=(0,0,1)]$. Furthermore, we assume that the absorption is moderate ($\alpha_s d \approx 0$, $\alpha_p d \approx 0$ with d being the interaction length), so that we can neglect the absorption terms in the coupled wave equations (12).

1. Transmission gratings

Transmission gratings are characterized by the condition $\cos\theta_S \cos\theta_P > 0$; both beams enter the crystal from a common face. By multiplying Eq. (12a) by $E_s^* n_s g_s$ and Eq. (12b) by $E_p^* n_p g_p$ and inserting the modulation ratio (8) we obtain

$$\frac{d}{dz}\widetilde{I_S}=\Gamma\frac{\widetilde{I_S}\,\widetilde{I_P}}{G\widetilde{I_S}+\widetilde{I_P}}, \tag{19a}$$

$$\frac{d}{dz}\widetilde{I_P}=-\Gamma\frac{\widetilde{I_S}\,\widetilde{I_P}}{G\widetilde{I_S}+\widetilde{I_P}}, \tag{19b}$$

where we have assumed $E_{sc,0}=iE_{sc,i}$ and Γ is the same exponential gain constant given in Eq. (16). We recall that the light intensities for the waves are given by $I=cEE^*ng$ with c being the speed of light. The intensities $\widetilde{I_S}\equiv I_S\cos\theta_S$ and $\widetilde{I_P}\equiv I_P\cos\theta_P$ appearing in Eqs. (19) correspond to the projections of the Poynting vectors along the surface normal $\hat{\zeta}$ and give the energy flow per unit area through a surface parallel to the input surface. The constant G depends on the geometry of interaction and is defined as

$$G=\frac{n_P g_P \cos\theta_P(\widehat{e^S}\cdot\vec{\kappa}\cdot\widehat{e^S})}{n_S g_S \cos\theta_S(\widehat{e^P}\cdot\vec{\kappa}\cdot\widehat{e^P})}. \tag{20}$$

By summing Eqs. (19a) and (19b) one recognizes that the total projected energy flow is conserved, that is $\widetilde{I_S}+\widetilde{I_P}\equiv\widetilde{I_0}$ is a constant. Therefore we have $d\widetilde{I_S}/\widetilde{I_S}+[G/(\widetilde{I_0}-\widetilde{I_S})]d\widetilde{I_S}=\Gamma dz$. Integration of this equation with the boundary conditions $\widetilde{I_S}(z=0)=\widetilde{I_{S0}}$, $\widetilde{I_P}(z=0)=\widetilde{I_{P0}}$ proper of the transmission grating geometry leads to the solution

$$\chi(z)=\chi_0 e^{\Gamma z}, \tag{21}$$

where

$$\chi(z)\equiv\frac{\widetilde{I_S}(z)}{[\widetilde{I_P}(z)]^G}\equiv\beta(z)[\widetilde{I_P}(z)]^{1-G}, \tag{22}$$

and $\chi_0=\chi(z=0)=(\widetilde{I_{S0}}/\widetilde{I_{P0}})\widetilde{I_{P0}}^{1-G}\equiv\beta_0\widetilde{I_{P0}}^{1-G}$. Therefore χ is a modified intensity ratio which for $G=1$ reduces to the conventional intensity ratio $\beta=\widetilde{I_S}/\widetilde{I_P}$. The evolution of the signal and pump wave intensities can then be expressed as

$$\widetilde{I_S}(z)=\widetilde{I_{S0}}\frac{1+\beta_0^{-1}}{1+\beta_0^{-1}\left(\dfrac{\widetilde{I_P}}{\widetilde{I_{P0}}}\right)^{1-G}}e^{-\Gamma z} \tag{23}$$

and

$$\widetilde{I_P}(z)=\widetilde{I_{P0}}\frac{1+\beta_0}{1+\beta_0\left(\dfrac{\widetilde{I_P}}{\widetilde{I_{P0}}}\right)^{G-1}}e^{\Gamma z}. \tag{24}$$

In the absence of photoexcitation anisotropy and for a nearly symmetric incidence of signal and pump beams the factor G is always very close to 1. In this case Eqs. (23) and (24) reduce to the well known conventional expressions derived for the isotropic case in symmetric configurations [25]. Note that for the case of transmission gratings considered here the factor G is bound to be positive because the tensor $\vec{\vec{\kappa}}$ contains only positive elements. We note also that, although for strong anisotropies the factor G may depart significantly from 1, in the above equations the influence of the term $(\widetilde{I_P}/\widetilde{I_{P0}})^{\pm(1-G)}$ on the beam intensities is still weaker than the one given by the exponential term. However, the corrections brought about by this term are not negligible. The saturation of the amplified signal beam to its maximum value is slower for $G>1$, and faster for $G<1$ than for the case $G=1$. This can be seen in Fig. 10 where $\widetilde{I_S}(z)/(\widetilde{I_{S0}}+\widetilde{I_{P0}})$ and $\widetilde{I_P}(z)/(\widetilde{I_{S0}}+\widetilde{I_{P0}})$ are plotted for different values of G and for a common value of the gain Γ. It is worth noticing that in the saturation region the depleted pump wave intensity decreases as $\widetilde{I_P}(z+\Delta z)=\widetilde{I_P}(z)\exp(-\Gamma\Delta z/G)$, as can be clearly recognized in Fig. 10. To get an impression of the possible range for the quantity G in a typical transmission geometry we may take first the example of a $BaTiO_3$ cut along the crystallographic axes and with both interacting beams entering the sample from air through the *a* face of the crystal. Considering all possible two-beam interaction geometries in such a configuration we have $0.936<G<1.07$ for $\kappa_{22}/\kappa_{33}=1$, $0.944<G<1.06$ for $\kappa_{22}/\kappa_{33}=0.1$, and $0.43<G<2.30$ for $\kappa_{22}/\kappa_{33}=10$. The ranges for $KNbO_3$ in the same kind of geometry are very similar. For crystals cut under 45° to the crystallographic axes, G varies between $G_{\min}\approx0.25$ and $G_{\max}\approx4$ for both $\kappa_{22}/\kappa_{33}=0.1$ and $\kappa_{22}/\kappa_{33}=10$.

2. Reflection gratings

In this case the signal and pump wave enter from opposite surfaces and one has $\cos\theta_S\cos\theta_P<0$. The coupled wave equations (12) can be brought again exactly in the form (19) if one allows one of the two projected intensities to take negative values. If we choose the signal wave to propagate towards positive z and the pump wave to propagate towards the negative z axis, then $\widetilde{I_S}(z)>0$ and $\widetilde{I_P}(z)<0$. Such a negative intensity value reflects the fact that the energy flow for the pump wave is in a direction which is opposite with respect to the considered surface orientation (vector $\hat{\zeta}$). Therefore the conserved quantity is still the sum of the (signed) intensities and the solution of the coupled equations (19) is still of the form given by Eqs. (21) and (22). However, the exponent G [still defined by (20)], is now bound to be a negative number. For a plate of thickness L the boundary values are now given at $z=0$ for the signal wave, and at $z=L$ for the pump wave. Using these boundary values in Eqs. (21) and (22) and reintroducing a positive intensity $|\widetilde{I_P}(z)|=-\widetilde{I_P}(z)$ for the pump wave one can easily find the expressions for the transmitted intensities $\widetilde{I_S}(z=L)$ and $|\widetilde{I_P}(z=0)|$, that is

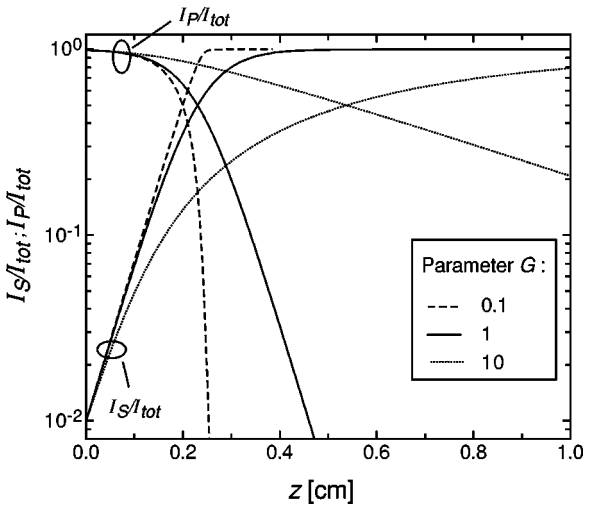

FIG. 10. Signal wave amplification and pump wave depletion as a function of the propagation distance z in transmission geometry. The normalized intensities $\widetilde{I_S}(z)/(\widetilde{I_{S0}}+\widetilde{I_{P0}})$ and $\widetilde{I_P}(z)/(\widetilde{I_{S0}}+\widetilde{I_{P0}})$ are plotted according to Eqs. (23) and (24) for $\Gamma=20\ \mathrm{cm}^{-1}$ and the three values of the factor G [Eq. (20)] given in the box.

$$\widetilde{I_S}(L)=\widetilde{I_S}(0)\frac{1+|\beta_0|^{-1}}{1+|\beta_0|^{-1}\left|\dfrac{\widetilde{I_P}(0)}{\widetilde{I_P}(L)}\right|^{1-|G|}}e^{-\Gamma L} \tag{25}$$

and

$$|\widetilde{I_P}|(0)=|\widetilde{I_P}|(L)\frac{1+|\beta_0|}{1+|\beta_0|\left|\dfrac{\widetilde{I_P}(0)}{\widetilde{I_P}(L)}\right|^{|G|-1}}e^{\Gamma L}, \tag{26}$$

which are in full analogy to Eqs. (23) and (24). The intensity ratio $|\beta_0|$ is defined here as $|\beta_0|\equiv\widetilde{I_S}(0)/|\widetilde{I_P}|(L)$ and differs

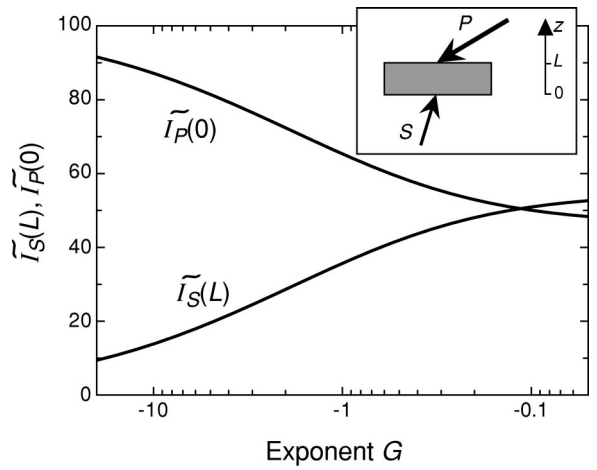

FIG. 11. Transmitted signal $[\widetilde{I}_S(L)]$ and pump intensity $[\widetilde{I}_P(0)]$ for reflection grating two wave mixing as a function of the exponent G. $G=-1$ corresponds to a fully symmetric and isotropic geometry. Parameters: gain coefficient $\Gamma=20\ \mathrm{cm}^{-1}$; sample thickness $L=0.2$ cm; input intensities $\widetilde{I}_S(0)=1$, $\widetilde{I}_P(L)=100$.

from the definition used for transmission gratings. For samples cut along the dielectric axes, symmetric interaction geometries, and in the absence of photoexcitation anisotropy, we have $G=-1$. In this case the two above expressions reduce to the well-known conventional relationships [26]. The correcting factor $|\widetilde{I}_P(0)/\widetilde{I}_P(L)|^{\pm(1-|G|)}$ brings about a similar influence on the output intensities as in the case of transmission gratings discussed above. Figure 11 shows an example of the G dependence of the signal and pump output intensities as obtained by solving the above transcendent equation. For fixed gain coefficient Γ an exponent G closer to 0 leads again to faster saturation.

VI. RESPONSE TIME AND SENSITIVITY

The photorefractive response time depends on several intrinsic and extrinsic material parameters and on the average photoconductivity of the material. The latter is a function of the power of the interacting beams and of the tensor $\vec{\kappa}$ describing the photoexcitation. In the simplest band transport model and in absence of applied electric fields the response time is expressed as [22,1]

$$\tau=\frac{\varepsilon_0\varepsilon_{eff}}{e\mu n_0}\,\frac{1+K^2/K_e^2}{1+K^2/K_0^2}, \tag{27}$$

where μ is the scalar mobility in direction of the grating vector $\vec{K}$ (modulus K), $K_0\equiv(e^2N_{eff}/\varepsilon_0\varepsilon_{eff}k_BT)^{1/2}$ is the Debye wave vector, and $K_e\equiv(e/k_BT\mu\tau_R)^{1/2}$ is the inverse diffusion length with τ_R being the free-carrier recombination time. The average density of free carriers n_0 can be written as a function of the amplitudes of the two interacting waves [21]. In the case where the pump wave is not depleted we have $n_0\propto|E_P|^2(\widehat{e_P}\cdot\vec{\kappa}\cdot\widehat{e_P})\tau_R$. Therefore the dielectric time $\tau_{die}\equiv(\varepsilon_0\varepsilon_{eff}/e\mu n_0)$ does depend on the light power,

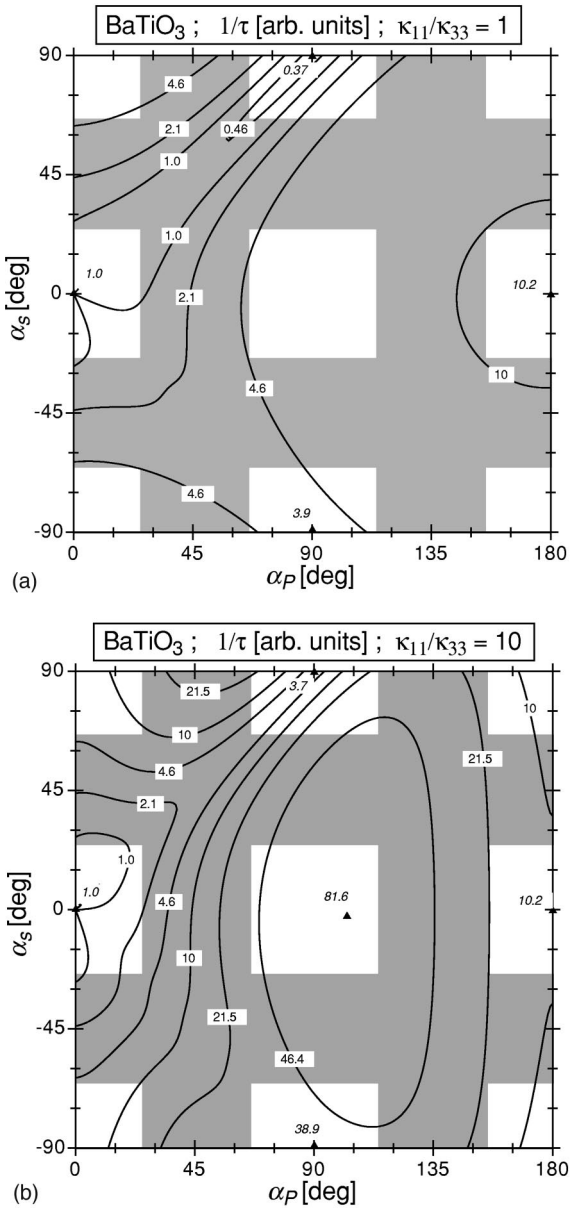

FIG. 12. Contour plot of the inverse photorefractive response time $1/\tau$ [Eq. (27)] for p-polarized beams in the ac plane of $BaTiO_3$ (undepleted pump). (a) Isotropic photoexcitation, $\kappa_{11}/\kappa_{33}=1$; (b) anisotropic photoexcitation $\kappa_{11}/\kappa_{33}=10$; The contour lines are at the indicated logarithmic distances. Parameters: effective density of traps $N_{eff}=10^{17}\ \mathrm{cm}^{-3}$, the inverse diffusion length in the c direction $K_e^{-1}=10$ nm. The values of $1/\tau$ are normalized to the inverse dielectric time $1/\tau_{die}$ for a grating pointing along the c axis $[=1/\tau(\alpha_p=\alpha_s=0°)]$.

on the polarization of the light waves and on the photoexcitation anisotropy through the free carrier density n_0, in addition it depends also on the direction of the grating vector $\hat{K}$ through the effective dielectric constant ε_{eff} and the mobility μ. For the response time τ additional dependencies on the grating direction $\hat{K}$ are brought about through the quantities K_0 and K_e.

As an example, in Figs. 12(a) and 12(b) we show the

predicted behavior of the inverse response time for hole conductive $BaTiO_3$. The dielectric and mobility anisotropies are taken from Refs. [10] and [13], respectively, while the effective number of traps and the diffusion length (for the charge movement along the c axis) are chosen as $N_{eff}=10^{17}$ cm^{-3} and $K_e^{-1}=10$ nm, respectively . We assume to be in the undepleted pump regime so that the photoconductivity is induced uniquely by the pump beam. Figure 12(a) is for $\kappa_{11}/\kappa_{33}=1$. The fastest response is predicted for $(\alpha_P,\alpha_S)=(180°,0°)$. This is for two reasons. On one hand the response is faster for counterpropagating than for copropagating beam geometries because in hole conducting $BaTiO_3$ the diffusion length is short [1], and therefore $K_e > K_0$ [see (27)]. On the other hand the position of the predicted maximum of $1/\tau$ corresponds to a counterpropagating geometry with wave vector $\hat{K}$ parallel to the a axis, which is favored with respect to other geometries [such as $(\alpha_P,\alpha_S)=(90°,-90°)$ with $\hat{K}\| c$ axis] because the large increase in mobility for charge movement along a overcomes the disadvantage of a larger effective dielectric constant. Figure 12(b) is for $\kappa_{11}/\kappa_{33}=10$. In this case the photoconductivity is larger for geometries having the pump wave polarized approximately along the a axis ($\alpha_P \approx 90°$) and the maximum is observed for a geometry for which the pump and signal wave are propagating nearly perpendicularly. Note that in the two graphs, the absolute values of the inverse response time $1/\tau$ are normalized to the inverse dielectric time $1/\tau_{die}(\hat{K}||c)$ for a wave vector parallel to the c axis. They are important only to judge the possible dynamic range of the response time among all possible interaction geometries. As might have been expected, the dynamic range increases in the case of anisotropic photoexcitation.

There are several possible definitions for the photorefractive sensitivity. Most of them measure the change per unit time of the refractive index or some related quantity such as the square root of the diffraction efficiency. For instance, a common definition is $S_n \equiv 1/I(\partial \Delta n/\partial t)$ evaluated at the time $t=0$ [1], with I being the incident light intensity. In the usual isotropic case the sensitivity S_n reaches its maximum if the pump and signal wave have equal intensities, because in this case the refractive index change modulation Δn is largest. It has to be noted that the sensitivity S_n cannot be significantly improved by an anistropy of the tensor $\vec{\kappa}$. The modulation depth m [Eq. (8)] cannot exceed the value of 1 and therefore the limiting physical process is basically the same as the one acting for the isotropic case. Another quantity which is proportional to the material sensitivity is given by the ratio Γ/τ between the exponential two-wave mixing gain and the response time [27]. It can easily be shown that for crystals following the simplest band model this measure is equivalent to the sensitivity S_n, provided that the photoexcitation tensor is isotropic. In contrast, in the anisotropic case significant deviations can be expected. As an example Fig. 13 shows the contour plots of the two-wave mixing sensitivity Γ/τ, again for hole conducting $BaTiO_3$ and with the same parameters used for Fig. 12. As before, the data in Figs. 13(a) and 13(b) are calculated for the undepleted pump regime and are normalized to a common dielectric relaxation time $\tau_{die}(\hat{K}||c)$

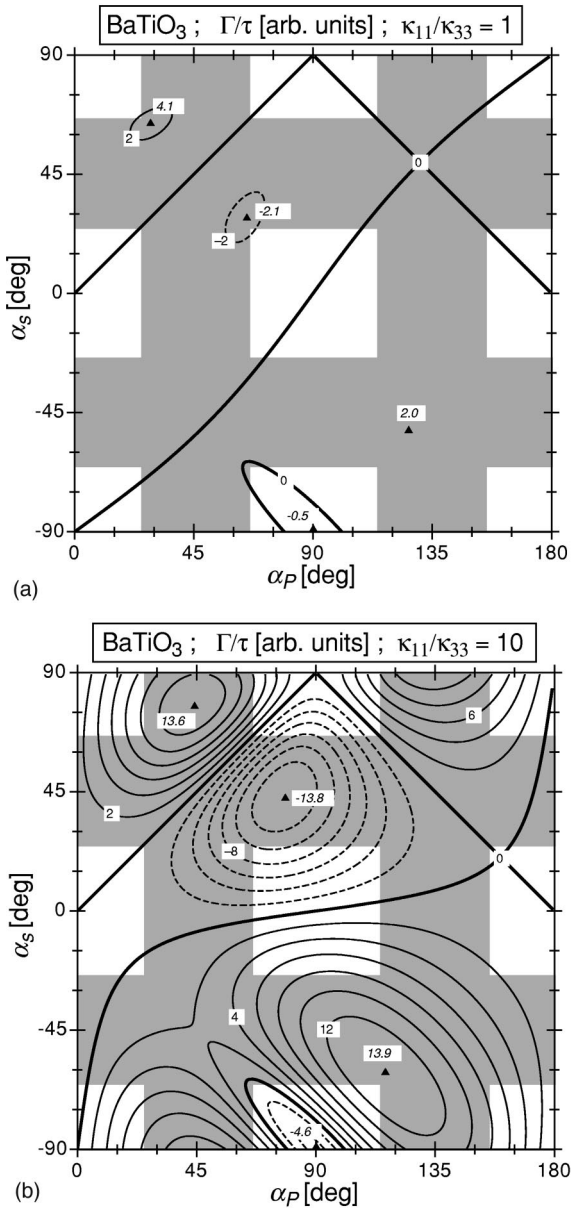

FIG. 13. Contour plot of the sensitivity $\Gamma \cos\theta_s/\tau$ for p-polarized beams in the ac plane of $BaTiO_3$ (undepleted pump). (a) $\kappa_{11}/\kappa_{33}=1$; (b) $\kappa_{11}/\kappa_{33}=10$. Parameters: $N_{eff}=10^{17}$ cm^{-3}, $K_e^{-1}(\hat{K}||c)=10$ nm. The values are normalized to a common inverse dielectric time $1/\tau_{die}$ for a grating pointing along the c axis $[=1/\tau(\alpha_p=\alpha_s=0°)]$.

for a grating in c-direction. By comparing Figs. 13(a) and 13(b) the effect of the anisotropy of the photoexcitation tensor is readily visible. It should be noted that the sensitivity can also be used to predict initial fanning directions at the onset of the illumination.

VII. CONCLUSIONS

We have discussed in detail the effects of the anisotropies of the dielectric constant, electro-optic effect, drift mobility, and photoexcitation cross section on photorefractive two-wave mixing. The example of the crystals $KNbO_3$ and

$BaTiO_3$ in the interaction plane of maximum photorefractive nonlinearity has shown clearly that the optimum geometries for maximum gain, shortest response time, or largest sensitivity are strongly dependent on all these anisotropies. The anisotropy of the photoexcitation process, often overlooked in the past, is shown to have a particularly strong influence. It allows us to obtain large gains even for geometries for which the interacting beams propagate nearly perpendicularly. Even though we have focused our attention on $KNbO_3$ and $BaTiO_3$, the expressions reported here apply to every nonoptically active photorefractive crystal as well. Therefore, upon determination of all necessary material parameters, the extension of this work to other materials is straightforward.

[1] P. Günter and J. P. Huignard, *Photorefractive Materials and their Applications I: Fundamental Phenomena* (Springer-Verlag, Berlin, 1988), Vol. 1.

[2] L. Solymar, D. J. Webb, and A. Grunnet-Jepsen, *The Physics and Applications of Photorefractive Materials* (Clarendon, Oxford, 1996), Vol. 11.

[3] J. Feinberg, Opt. Lett. **7**, 486 (1982).

[4] J. P. Huignard and J. P. Herriau, Appl. Opt. **16**, 1807 (1977).

[5] S. MacCormack, G. D. Bacher, J. Feinberg, S. O'Brien, R. J. Lang, M. B. Klein, and B. A. Wechsler, Opt. Lett. **22**, 227 (1997).

[6] G. C. Valley, J. Opt. Soc. Am. B **4**, 14 (1987); **4**, 934(E) (1987).

[7] H. Y. Zhang, X. H. He, E. Chen, Y. Liu, S. H. Tang, D. Z. Shen, and D. Y. Jiang, Appl. Phys. Lett. **57**, 1298 (1990).

[8] C. Medrano, M. Zgonik, S. Berents, P. Bernasconi, and P. Günter, J. Opt. Soc. Am. B **11**, 1718 (1994).

[9] M. Zgonik, R. Schlesser, I. Biaggio, E. Voit, J. Tscherry, and P. Günter, J. Appl. Phys. **74**, 1287 (1993).

[10] M. Zgonik, P. Bernasconi, M. Duelli, R. Schlesser, P. Günter, M. H. Garrett, D. Rytz, Y. Zhu, and X. Wu, Phys. Rev. B **50**, 5941 (1994).

[11] C. P. Tzou, T. Y. Chang, and R. W. Hellwarth, Proc. SPIE **613**, 58 (1986).

[12] D. Mahgerefteh, D. Kirillov, R. S. Cudney, G. D. Bacher, R. M. Pierce, and J. Feinberg, Phys. Rev. B **53**, 7094 (1996).

[13] P. Bernasconi, I. Biaggio, M. Zgonik, and P. Gunter, Phys. Rev. Lett. **78**, 106 (1997).

[14] A. A. Izvanov, A. E. Mandel, N. D. Khatkov, and S. M. Shandarov, Optoelectronics Data Processing Instrumentation **2**, 80 (1986).

[15] S. I. Stepanov, S. M. Shandarov, and N. D. Khatkov, Fiz. Tverd. Tela (Leningrad) **29**, 3054 (1987) [Sov. Phys. Solid State **29**, 1754 (1987)].

[16] P. Günter and M. Zgonik, Opt. Lett. **16**, 1826 (1991).

[17] G. Pauliat, M. Mathey, and G. Roosen, J. Opt. Soc. Am. B **8**, 1942 (1991).

[18] D. F. Nelson and M. Lax, Phys. Rev. Lett. **24**, 1187 (1970).

[19] G. Montemezzani and M. Zgonik, Phys. Rev. E **55**, 1035 (1997).

[20] M. Zgonik, K. Nakagawa, and P. Günter, J. Opt. Soc. Am. B **12**, 1416 (1995).

[21] G. Montemezzani, C. Medrano, P. Günter, and M. Zgonik, Phys. Rev. Lett. **79**, 3403 (1997).

[22] N. V. Kukhtarev, V. B. Markov, S. G. Odulov, M. S. Soskin, and V. L. Vinetskii, Ferroelectrics **22**, 949 (1979).

[23] K. Buse, Appl. Phys. B: Lasers Opt. **64**, 273 (1997).

[24] G. Montemezzani, A. A. Zozulya, L. Czaia, D. Z. Anderson, M. Zgonik, and P. Günter, Phys. Rev. A **52**, 1791 (1995).

[25] N. V. Kukhtarev, V. B. Markov, S. G. Odulov, M. S. Soskin, and V. L. Vinetskii, Ferroelectrics **22**, 961 (1979).

[26] P. Yeh, Opt. Commun. **45**, 323 (1983).

[27] D. Rytz, M. B. Klein, R. A. Mullen, R. N. Schwartz, G. C. Valley, and B. A. Wechsler, Appl. Phys. Lett. **52**, 1759 (1988).